J Mater Sci (2009) 44:5095–5101
DOI 10.1007/s10853-009-3697-z

FERROELECTRICS

Defect-induced asymmetry of local hysteresis loops on $BiFeO_3$ surfaces

Peter Maksymovych · Nina Balke · Stephen Jesse · Mark Huijben · Ramamoorthy Ramesh · Arthur P. Baddorf · Sergei V. Kalinin

Received: 26 May 2009 / Accepted: 16 June 2009 / Published online: 2 July 2009

Abstract Local piezoresponse hysteresis loops were systematically studied on the surface of ferroelectric thin films of $BiFeO_3$ grown on $SrRuO_3$ and $La_{0.7}Sr_{0.3}MnO_3$ electrodes and compared between ultrahigh vacuum and ambient environment. The loops on all the samples exhibited characteristic asymmetry manifested in the difference of the piezoresponse slope following local domain nucleation. Spatially resolved mapping has revealed that the asymmetry is strongly correlated with the random-field disorder inherent in the films and is not affected by the random-bond disorder component. The asymmetry thus originates from electrostatic disorder within the film, which allows using it as a unique signature of single defects or defect clusters. The electrostatic effects due to the measurement environment also contribute to the total asymmetry of the piezoresponse loop, albeit with a much smaller magnitude compared to local defects.

P. Maksymovych (✉) · N. Balke · S. Jesse · A. P. Baddorf · S. V. Kalinin
Center for Nanophase Materials Sciences, Oak Ridge National Laboratory, Oak Ridge, TN 37831, USA
e-mail: maksymovychp@ornl.gov

M. Huijben · R. Ramesh
Departments of Materials Sciences and Engineering, and Physics, University of Califronia Berkeley, Berkeley, CA 94720, USA

M. Huijben
Faculty of Science and Technology, MESA+ Institute for Nanotechnology, University of Twente, P.O. Box 217, 7500 AE Enschede, The Netherlands

Introduction

Current interest in nanoscale ferroelectric materials is stimulated by their potential uses in conventional as well as new ferroelectric applications, such as nanoactuators, high-k dielectrics, supercapacitors, memory, and spintronic devices [1–4]. In some of these applications, the exquisite control of the ferroelectric order parameter will enable new functionality via multiferroic coupling to other order parameters (e.g., magnetic, ferroelastic) [5, 6]. From a fundamental perspective, ferroelectric switching is also a model system to study size effects and domain wall dynamics of reversible phase transitions in a double-well potential [7, 8]. Notably, most theoretical models for ferroelectric materials and polarization domain structures, as well as the derivative device concepts, are developed for defect-free materials. At the same time, real-life ferroelectric thin films of mostly perovskite oxides are notoriously imperfect both chemically and structurally, due to the non-equilibrium growth conditions, oxygen chemistry, and strain relaxation [9]. The defects, such as lattice dislocations, space charge regions, and vacancy gradients, couple to the ferroelectric order parameter via electrostatic and strain fields, affecting the magnitude of ferroelectric polarization and its switching by the external electric field [10, 11]. The peculiar and application-relevant properties of relaxor ferroelectrics, such as strong frequency dispersion and dielectric response, are believed to arise from substitutional charge disorder that produces quenched electric random fields in the material [12]. It is therefore necessary to seek new ways of revealing the presence of defect centers and understand their role in both local and macroscopic polarization switching.

Scanning probe microscopy offers a unique opportunity to address the role of localized defects, by utilizing a strong

electrostatic field of a sharp metal probe to confine ferroelectric switching in the nanoscale volume under the probe. The local hysteresis loop is thus determined by the nucleation and growth of a single domain [13], rather than a collective effect of domain nucleation and domain wall motion as in macroscopic switching studies. Two recent trends in mapping of defect centers using SPM include piezoresponse force microscopy of buried ferroelectric films through a top macroscopic electrode and direct mapping of local hysteresis loops on ferroelectric surfaces. Using the former approach, it was possible to demonstrate the inhomogeneity of macroscopic ferroelectric switching, locate the nucleation centers, and quantitatively characterize domain wall motion [14–16]. Local hysteresis loops provide complementary information, since they directly probe local nucleation dynamics of a single or few domains under the tip at a surface location that may or may not contain a defect. One can thus establish the mechanism of single-domain nucleation [17] and explore the effects of charged defects [18], ferroelastic domain walls [19], and grain boundaries [20] on the nucleation and subsequent growth of a reversely polarized domain.

Here, we discuss systematic changes in local hysteresis loops measured on the surface of epitaxial thin films of $BiFeO_3$ under varying electrostatic boundary conditions. Local electric fields originate from the inherent disorder in the ferroelectric film, while the average built-in field across the film is varied through the choice of the bottom electrode and/or measurement environment. Our main finding is that the built-in fields induce the asymmetry of the local hysteresis loops, between the forward and reverse switching directions. This is a distinct signature of single defects, which is complementary to a recently discovered fine structure in the hysteresis loops [18].

Experimental

The measurements have been carried out using a recently developed ultrahigh vacuum piezoresponse force microscope, with Pt-coated cantilevers (Mikromasch, CSC37) [17]. Hysteresis loops of out-of-plane piezoresponse were acquired using band-excitation piezoresponse force spectroscopy [21]. The statistics of the hysteresis loops were obtained on two different samples—a 200 nm film of $BiFeO_3$(100) grown on $SrRuO_3$ (SRO)/$SrTiO_3$ (STO) and a 50 nm $BiFeO_3$(100) grown on $LaSrMnO_3$ (LSMO)/STO support. Both samples were grown by pulsed laser deposition, exhibited flat topography in AFM, and were confirmed to have high epitaxial quality by X-ray scattering. The out-of-plane polarization domain structure was predominantly monodomain with downward polarization direction (toward the bottom electrode) similar to previous studies [17, 22]. The effect of 71° and 109° in-plane domain walls on the hysteresis loops was undetectable in our experiments, given the relatively small spatial resolution of the grids used to map the variations of the loops across the surface. Each hysteresis loop was fit using a phenomenological function [19] to determine nucleation and growth parameters systematically. The nucleation bias (U_{PN} for positive and U_{NN} for negative) was estimated at the 3% of the total change in the local piezoresponse at the onset of switching, while the coercive bias (U_c) at 50% of the signal.

Results

Figure 1 compares average hysteresis loops obtained from three investigated samples/conditions along with the distribution of the nucleation biases extracted from the individual loops. The main effect of the vacuum environment is to change the loop imprint from $\sim$0 V in air to -1.0 V in vacuum for the 200 nm BFO/SRO sample (Fig. 1a) and a similar shift of 0.6 V for the 50 nm BFO/LSMO sample (Fig. 1c). The imprint, estimated as $\langle U_{PN} - |U_{NN}|\rangle/2$, is a measure of the macroscopic built-in potential across the film. The changes of the built-in potential with the measurement environment clearly identifies its interfacial origin [23], which is characteristic of thin films and distinct from bulk dipole reorientation, often suggested to be the case for thicker samples and single crystals [9]. This is further confirmed by observing that a similar effect occurs when the material of the bottom electrode is changed from SRO to LSMO, Fig. 1. Notably, this illustrates that the imprint can be controlled by the combination of environment and bottom electrode materials, and can be almost entirely compensated as in the case of BFO/SRO sample in air and BFO/LSMO sample in vacuum.

In order to compare the effect of the built-in field on the local switching, we mapped the hysteresis loops on a grid with a typical dimension of 1×1 μm^2 and a resolution from 20 to 200 nm. The variation among the loops was analyzed against three phenomenological parameters: (1) random-field component, $U_{RF} = (U_{PN} - |U_{NN}|)/2$; (2) random-bond component, $U_{RB} = (U_{PN} + |U_{NN}|)/2$; and (3) the slope of the hysteresis curve following nucleation, $r_s = [d_{eff}(U_C) - d_{eff}(U_N)]/[U_C - U_N]$, where $d(U)$ is the remanent local piezoresponse along the hysteresis loop, U_N is the nucleation bias; and (3) the asymmetry of the loop, $A = r_s^+/r_s^-$, estimated as the ratio of slopes on the forward (+) and backward (−) branches of the hysteresis loop (Fig. 2a–c).

The loop asymmetry varied by about an order of magnitude within the datasets taken on each sample in ambient and vacuum environments (Figs. 2e and 3a). From the

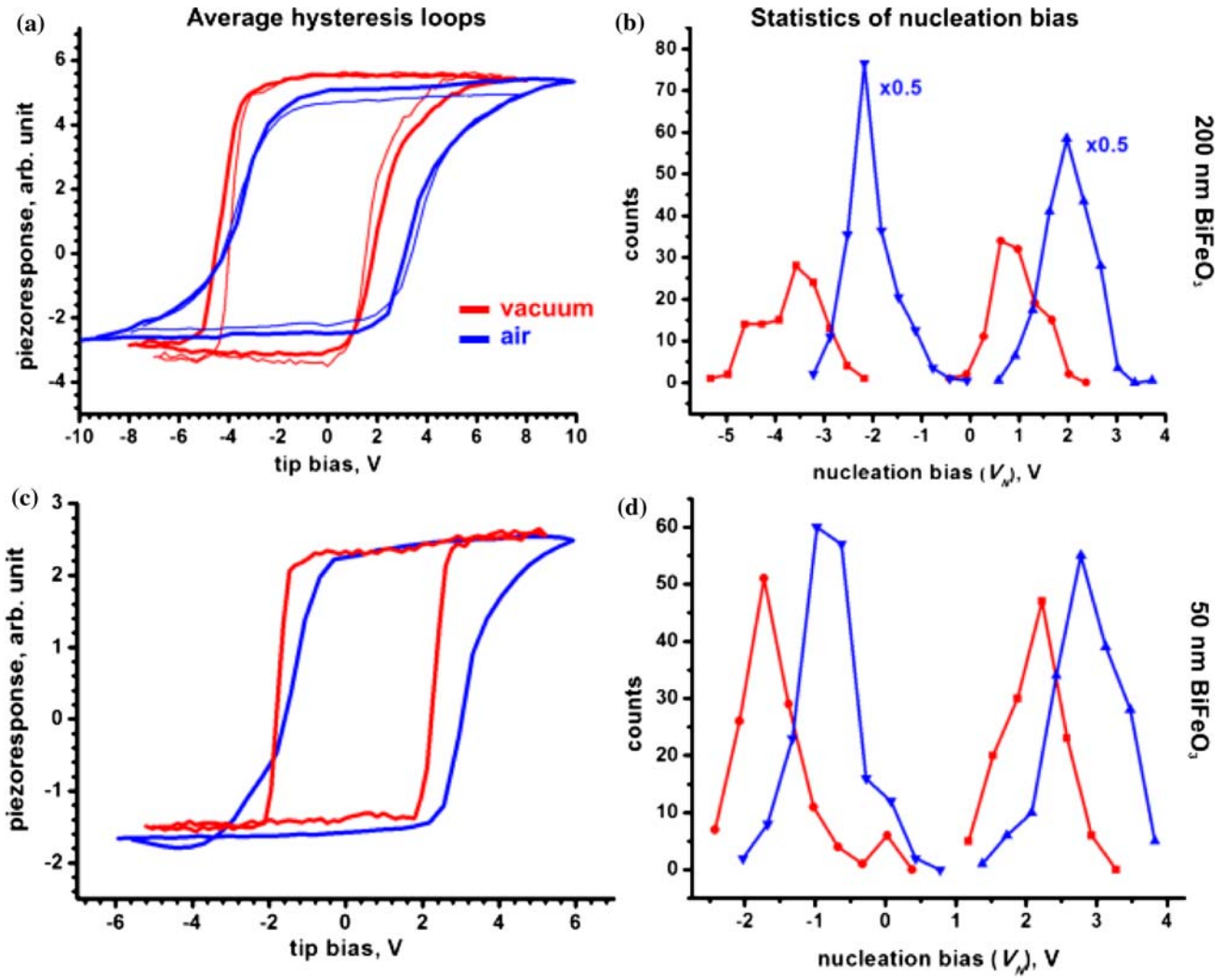

Fig. 1 Average piezoresponse hysteresis loops acquired on **a** the 200-nm $BiFeO_3/SrRuO_3$ sample and **c** the 50 nm $BiFeO_3/La_{0.7}Sr_{0.3}MnO_3$. **b** and **d** Corresponding statistics of the nucleation bias. Blue curves correspond to ambient environment and red to ultrahigh vacuum ($p_0 = 2 \times 10^{-10}$ Torr). Vacuum measurements were carried out without any surface cleaning following the introduction of the sample into the measurement chamber. (Color figure online)

comparison of three datasets, we established the following trends:

(1) The asymmetry is strongly correlated to the random-field disorder in the film (Figs. 2d, e and 3a) and shows no correlation to the random-bond disorder (Figs. 2e, f and 3b). The correlation with the random-field can be approximately described by $\log(A) = a_0 + bU_{RF}$. This relationship is likely to deviate from a simple exponential. It is justified here because the experimental values are obtained in a limited range of the random-potential fluctuations within the material and a relatively large scatter, and so only qualitative conclusions can be derived.

(2) The built-in potential has little effect on the slope b, i.e., the variation of loop asymmetry within each dataset. This is seen from a similarity of the respective correlations in vacuum and air (Fig. 3a), as well as among the samples grown on different electrodes. Notably, the magnitude of change of the built-in potential is comparable to random-field fluctuations.

(4) Although the effect of the built-in potential is minimal within each dataset, there is a noticeable trend toward preferred asymmetry with the sign and the magnitude of the built-in potential (Fig. 3a). The median of the asymmetry distributions for each sample reveals that the loop has an average asymmetry of 0.1 in 200 nm $BiFeO_3$ film in vacuum, increasing to 0.7 in air and to 1.5 for the LSMO electrode.

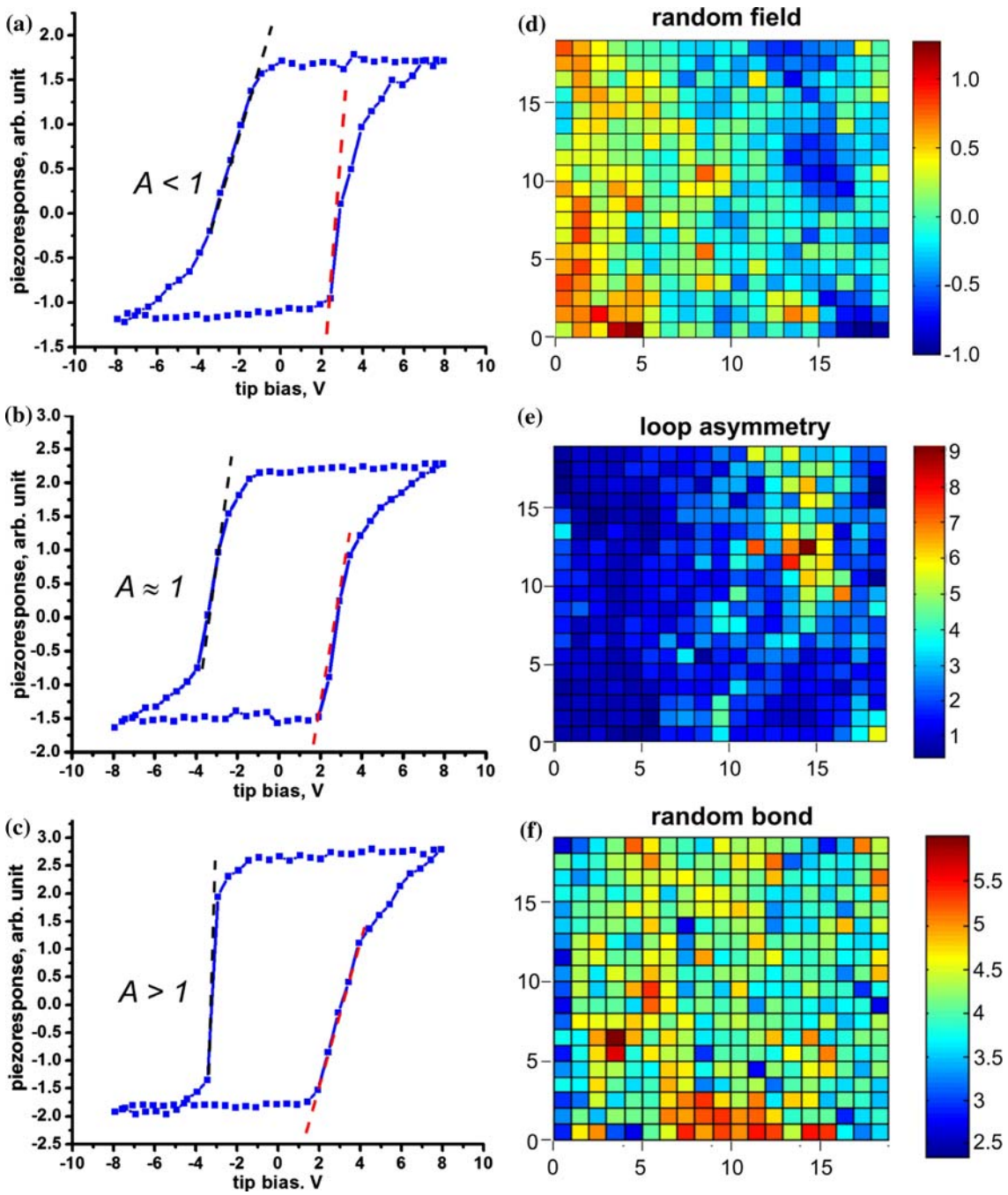

Fig. 2 **a–c** Representative hysteresis loops acquired on the 200 nm $BiFeO_3/SrRuO_3$ in ambient, showing three types of asymmetry observed within a single dataset. Spatial distribution of random-field component U_{RF} (**d**), loop asymmetry A (**e**), and random-bond component U_{RB} (**f**) based on 400 hysteresis loops acquired on a grid with dimensions 400 × 400 nm^2

(5) The spatial variation of the asymmetry is not uniform, revealing one or several hot-spots across the sampling grid (Fig. 2d, e). These hot-spots are not observed in random-bond fluctuations (U_{RB}), Fig. 2f, but closely match those in the random-field (U_{RF}), Fig. 2d.

A direct correlation between asymmetry and random-field fluctuations as well as a detectable dependence on the magnitude and sign of the built-in field inadvertently points to the electrostatic origin of the loop asymmetry. Since the local loops within a single map are acquired with the same parameters for switching spectroscopy, such as the tip-contact area and the magnitude of the AC bias used to probe local piezoresponse, the observed asymmetry and disorder is not caused by instrumental artifacts. The

hot-spots which produce the most dramatic change in the RF component must therefore originate from charged defects [19]. These defects are very long range (10–100 nm) if we consider each hot-spot in Fig. 2d as one or several defects, and are therefore likely to be charged core dislocations or other extended defects.

Discussion

The built-in potential

Although the microscopic origin of the interfacial processes leading to the occurrence of the built-in potential (e.g., chemisorption of adsorbates, ionicity of adsorbed water, surface reconstruction, etc.) are still undetermined, the effect can be rationalized if we consider semiconducting properties of the ferroelectric film as suggested before [23]. In brief, the formation of a Schottky contact with the bottom electrode and presence of uncompensated charges on the surface of the ferroelectric film creates regions of space charge within the film. The maximum built-in electric field at the interface (E_{bi}) is related to the built-in potential (V_{bi}) as $E_{bi} = \sqrt{\frac{2eN_{eff}}{\varepsilon_0 \kappa}} V_{bi}$ [23], where N_{eff} is the total density of screening charges in the material (including shallow and possible deep levels) and κ, is the dielectric constant of the ferroelectric with an estimated value of $\sim 6 \times 10^7$ V/cm for model parameters of $N_{eff} = 10^{19}$ cm^{-3}, $\kappa = 100$, and $V_{bi} = 1$ V. This is a large enough magnitude to cause a substantial effect on the thermodynamics of nucleation, and it is comparable to the tip-induced electric fields in the PFM experiment, $\sim 10^{7-8}$ V/cm. The transition from vacuum to ambient environment is likely to be associated with the change of the surface charge (due to the presence of water, its partial dissociation, and ionic adsorption [24]), which will affect the depletion width and the resulting built-in field. The bottom electrode factors into V_{bi} through the properties of the Schottky barrier, influenced by the work function and electronegativity of the metallic oxides [25], and the interfacial chemistry with the ferroelectric [26]. The effect of the bottom electrode will be significant only when the film thickness is comparable or less than the depletion width in the material. Notably, the average width of the hysteresis loop $(\langle U_{PN} \rangle + \langle |U_{NN}| \rangle)/2$ does not change appreciably upon transition from vacuum to ambient. This implies that screening of polarization charge, which strongly contributes to the activation barrier to domain nucleation [13] and the width of the loop, is intrinsic, involving vacancies, shallow levels, and strongly bonded adsorbates in the material, and has small dependence on the environment in our measurements.

Loop asymmetry

In order to interpret the physical mechanism by which the loop becomes asymmetric, one needs to consider that the local piezoresponse represents the weighted average of the elastic deformation of the ferroelectric surface driven by the tip's electric field, with the elastic Green's function as the weighting factor [13, 27]. When a domain of opposite polarization is nucleating under the tip, the effective piezoresponse can be approximated by [13]

$$d_{eff} \approx u_0 + \frac{3}{4} d_{33} \frac{\pi \cdot z_{im} - 8r}{\pi \cdot z_{im} + 8r} + \frac{(1+4\nu)}{4} d_{31} \frac{\pi \cdot z_{im} - 8r}{\pi \cdot z_{im} + 8r} + \frac{1}{4} d_{15} \frac{3\pi \cdot z_{im} - 8r}{3\pi \cdot z_{im} + 8r}, \quad (1)$$

where z_{im} is the descriptor of the potential under the tip (in the image-charge approximation), r is the domain radius, d_{ij} are the piezoelectric constants of the material, ν is the Poisson ratio, u_0 is the offset due to long-range electrostatics and instrumental artifacts. The local piezoresponse thus changes between the constant values of $u_0 \pm \frac{1}{4}(3d_{33} + (1+4\nu)d_{31} + d_{15})$ when the domain size grows from zero (+ sign) to infinite (− sign). In the idealized condition of the alignment of the tip and domain axes, as well as a cylindrical symmetry of the problem, the slope of the hysteresis curve is a non-trivial, but direct measure of growth rate of a single domain under the tip. In particular, for a rigid ferroelectric model, one can show that for critical values of the nucleus radius [19] (i.e., right after nucleation)

$$r_c = \frac{\pi \psi_S z_{im} \gamma}{2P_S(U_c \pm 2 z_{im} \gamma E_b)} \text{ and tip bias, } U_c \approx 4\sqrt{\frac{\psi_S z_{im} \gamma}{3\varepsilon_0(\kappa+1)}}, \quad (2)$$

the slope is given by

$$\left[\frac{\partial d_{eff}}{\partial U}\right]_c \approx \frac{16 r_c \pi z_{im}}{(U_c \pm 2 z_{im} \gamma E_b)} \left[\frac{d_{33}^*}{(\pi \cdot z_{im} + 8r_c)^2} + \frac{3 d_{15}^*}{4(3\pi \cdot z_{im} + 8r_c)^2}\right], \quad (3)$$

where γ is the dielectric anisotropy, P_S is the spontaneous polarization, ψ_s is the domain wall energy, E_b is the built-in field, and κ is the dielectric constant, $d_{33}^* = \frac{1}{4}(3d_{33} + (1+4\nu)d_{31})$. The choice between the plus or minus sign in Eqs. 2 and 3 is determined by whether the direction of the built-in field is coincident or opposite to the direction of the tip potential, respectively. The estimated critical radius of the nucleus and the slope of the hysteresis loop as a function of the built-in field are plotted in Fig. 3c. The

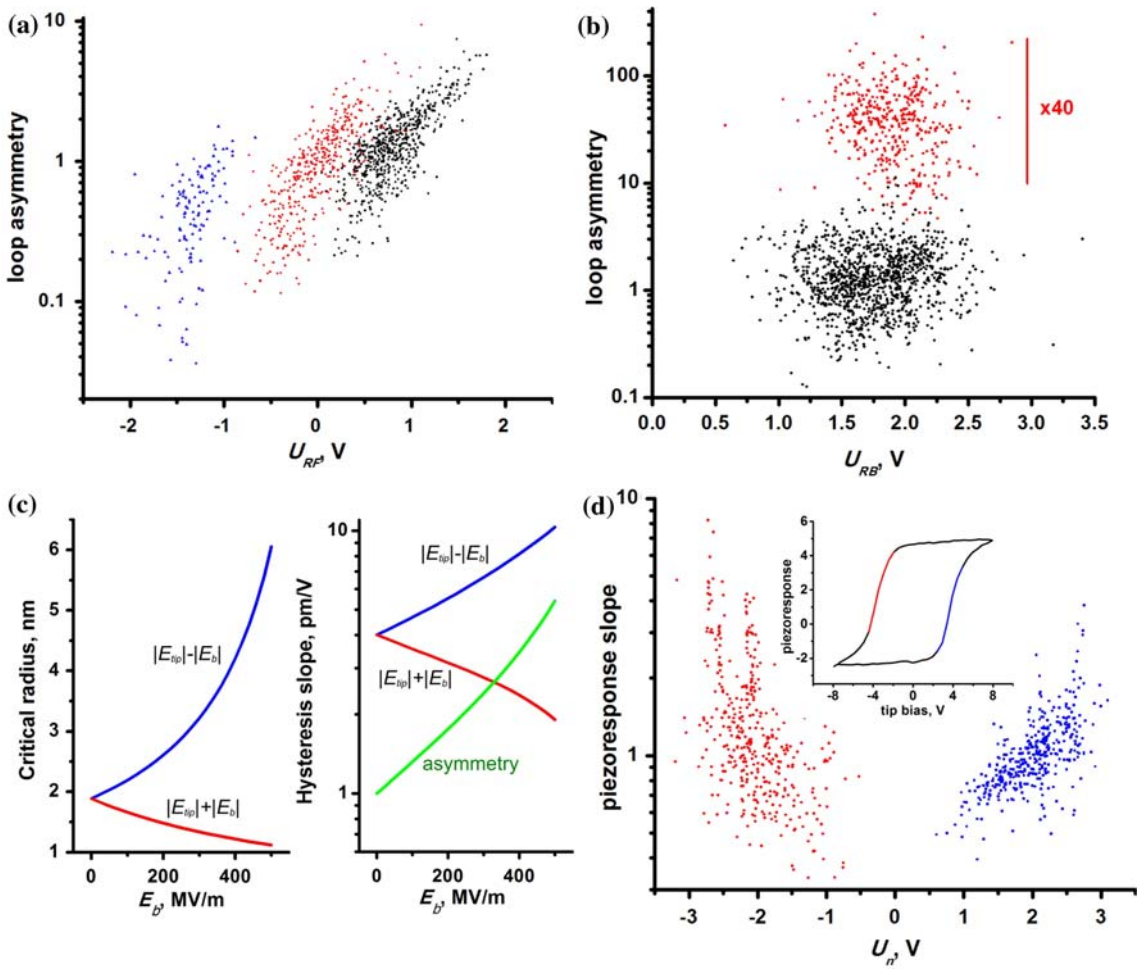

Fig. 3 Loop asymmetry as a function of the random-field (**a**) and random-bond (**b**) bias. The colors correspond to the 200 nm BFO/SRO sample in vacuum (blue), 200 nm BFO/SRO sample in air (red), and 50 nm BFO/LSMO sample in air (black). **c** Critical bias and slope of the hysteresis loops estimated using Eqs. 2 and 3, respectively, using the following values for parameters: $\psi_s = 0.35$ J/m^2, $d^*_{33} = 50$ pm/V, $d^*_{15} = 20$ pm/V, $\kappa = 20$ and $z_{im} = 5$ nm; blue and red lines are for positive and negative sign in Eqs. 2 and 3, respectively, and green line is the estimated asymmetry; **d** the slope of local piezoresponse as a function of the nucleation bias for the 200 nm BFO/SRO film in air. The inset in (**d**) shows the regions of the hysteresis loop used to extract the corresponding slopes. (Color figure online)

hysteresis slope does indeed scale significantly with the magnitude of the built-in field. In addition, the built-in potential makes the size of the critical nuclei different at the positive and negative branches of the hysteresis loop, as was suggested in our previous publication [17]. Notably, the nucleus size is smaller if the sign of the built-in potential coincides with the sign of the tip potential (+ in Eq. 3). Under the same conditions, the slope at the critical bias is also *smaller*. This particular feature is in good agreement with the overall shape of the asymmetric hysteresis loops on $BiFeO_3$. For example, as seen in Fig. 2a–c, the smaller nucleation bias of the imprinted loop is followed by a slower saturation of the piezoresponse signal (i.e., smaller slope), while the other branch saturates much faster.

The correlation between the slope of each hysteresis loop and the respective nucleation bias is statistically reproducible as seen in Fig. 3d for the ambient dataset acquired on the 200 nm $BiFeO_3/SrRuO_3$ sample. It is thus clear why the loop asymmetry correlates strongly with the random-field defects and does so insignificantly with the random-bond defects. Indeed, the ratio of the slopes between the forward and backward branches of the hysteresis loop will be maximized if the increase in the magnitude of one nucleation bias coincides with the corresponding decrease of the other nucleation bias. Random-bond defects change the depth of the double-well potential, thus increasing or decreasing the magnitudes of both nucleation biases. This will correspondingly change the forward and backward slopes of the hysteresis loop, but

their ratio will remain the same or change very little. We would like to point out that although spatially resolved maps of loop asymmetry and U_{RF} contain essentially the same information, observation of a single non-zero U_{RF} value is, by itself, not sufficient to judge the presence of the random-field defect, since this value also includes the macroscopic built-in potential. The asymmetry can, however, be extracted even from a single loop, and it also reflects local thermodynamics of domain nucleation in the presence of a charged defect.

The model of a perfect alignment between the nucleating domain and cylindrical tip is likely oversimplified, particularly in the presence of a charged defect. According to a recent analysis within the rigid model [18, 28], localized defects can cause a very strong deviation of both the shape and the location of the nucleating domain. In this case, the slope of the hysteresis loop cannot be interpreted as simply as growth rate of the domain, and the comparison requires detailed calculations. The sign of the charge localized on the defect breaks the symmetry of the nucleation process for the forward and backward branches, with the defect being a nucleation center for one orientation of the domain and the tip apex for the other. The asymmetry of the hysteresis loop in this case will be significantly amplified, since the local piezoresponse originates from very different spatial distributions of the ferroelectric order parameter. This additional source of asymmetry may explain why the effect of localized random-field disorder is significantly more pronounced (by about an order of magnitude) compared to the changes in the delocalized built-in potential, Fig. 3a.

Conclusions

In summary, we have determined that both delocalized built-in field, arising from the inequivalent interfaces of the ferroelectric film, and the localized fields produced by charged defects inherent in ferroelectric films are manifested as the asymmetry of hysteresis loops measured locally by piezoresponse force spectroscopy. The loop asymmetry arises from the difference in forward and backward dynamics of single domain nucleation in the presence of the built-in field. The effect of local fields is much more pronounced than that of a macroscopic built-in field, which we suggest to be due to an additional difference in the spatial location of the forward and backward nucleus in the presence of a charged defect. Since we have also observed asymmetric loops on epitaxial $Pb(Zr_{0.2}Ti_{0.8})O_3$ samples grown on LSMO electrodes (not shown), we believe that the conclusions of this article are not restricted to $BiFeO_3$. Identifying the role of defects in the ferroelectric switching is crucial from both fundamental and applied perspectives, since the defects can either deteriorate the performance of thin film devices, or on the contrary be used to control them. Charged defects are of particular importance for doped ferroelectric and multiferroic films, which are currently investigated because of the possibility to tune the band gap and strain of the material via doping, potentially enabling new energy-related applications.

Acknowledgements The research of PM was performed as a Eugene P. Wigner Fellow and staff member at the Oak Ridge National Laboratory. The experiments were conducted at the Center for Nanophase Materials Sciences, Office of Basic Energy Sciences, U.S. Department of Energy.

References

1. Tsymbal EY, Kohlstedt H (2006) Science 313:181
2. Scott JF (2007) Science 315:954
3. Maksymovych P, Jesse S, Yu P, Ramesh R, Baddorf AP, Kalinin SV (2009) Science 324:1421
4. Gajek M, Bibes M, Fusil S, Bouzehouane K, Fontcuberta J, Barthélémy A, Fert A (2007) Nat Mater 6:296
5. Cheong S-W, Mostovoy M (2007) Nat Mater 6:13
6. Ramesh R, Spaldin NA (2007) Nat Mater 6:21
7. Kalinin SV et al (2008) Mater Today 11:16
8. Paruch P, Giamarchi T, Triscone J-M (2007) Topics Appl Phys 105:339
9. Damjanovic D (1998) Rep Prog Phys 61:1267
10. Tagantsev AK (1996) Ferroelectrics 184:79
11. Ahluwalia R, Gao W (2000) Phys Rev B 63:012103
12. Kleemann W (2006) J Mater Sci 41:129. doi:10.1007/s10853-005-5954-0
13. Morozovska AN, Kalinin SV, Eliseev EA, Svechnikov SV (2007) Ferroelectrics 354:198
14. Gruverman A. J Mater Sci. doi:10.1007/s10853-009-3623-4
15. Gruverman A, Wu D, Scott JF (2008) Phys Rev Lett 100:097601
16. Jo JY, Yang SM, Kim TH, Lee HN, Yoon J-G, Park S, Yo J, Jung MH, Noh TW (2009) Phys Rev Lett 102:045701
17. Maksymovych P, Jesse S, Huijben M, Ramesh R, Morozovska A, Baddorf AP, Kalinin SV, Maksymovych P, Jesse S, Huijben M, Ramesh R, Morozovska A, Baddorf AP, Kalinin SV et al (2009) Phys Rev Lett 102:017601
18. Kalinin SV et al (2008) Phys Rev Lett 100:155703
19. Jesse S et al (2008) Nat Mater 7:209
20. Rodriguez BJ et al (2009) Adv Funct Mater 19:1
21. Jesse S, Maksymovych P, Kalinin SV (2008) Appl Phys Lett 93:112903
22. Zavaliche F, Das RR, Kim DM, Eom CB, Yang SY, Shafer P, Ramesh R (2005) Appl Phys Lett 87:182912
23. Tagantsev AK, Gerra G (2006) J Appl Phys 100:015607
24. Fong DD, Kolpak AM, Eastman JA, Streiffer SK, Fuoss PH, Stephenson GB, Thomposon C, Kim DM, Choi KJ, Eom CB, Grinberg I, Rappe AM (2006) Phys Rev Lett 96:127601
25. Sze SM (1997) Modern semiconductor device physics. Wiley-Interscience
26. Stengel M, Vanderbilt D, Spaldin NA (2009) Nat Mater 8:392
27. Karapetian E, Sevostianov I, Kachanov K (2000) Philos Mag B 80:4
28. Morozovska AN et al (2008) Phys Rev B 78:054101